J. Fluid Mech. (2019), *vol.* 872, *pp.* 729–751. © Cambridge University Press 2019
doi:10.1017/jfm.2019.416

Richtmyer–Meshkov instability on a quasi-single-mode interface

Yu Liang[1], **Zhigang Zhai**[1,†], **Juchun Ding**[1] **and Xisheng Luo**[1]

[1]Advanced Propulsion Laboratory, Department of Modern Mechanics, University of Science and Technology of China, Hefei 230026, China

(Received 28 November 2018; revised 15 May 2019; accepted 16 May 2019; first published online 13 June 2019)

Experiments on Richtmyer–Meshkov instability of quasi-single-mode interfaces are performed. Four quasi-single-mode air/SF_6 interfaces with different deviations from the single-mode one are generated by the soap film technique to evaluate the effects of high-order modes on amplitude growth in the linear and weakly nonlinear stages. For each case, two different initial amplitudes are considered to highlight the high-amplitude effect. For the single-mode and saw-tooth interfaces with high initial amplitude, a cavity is observed at the spike head, providing experimental evidence for the previous numerical results for the first time. For the quasi-single-mode interfaces, the fundamental mode is the dominant one such that it determines the amplitude linear growth, and subsequently the impulsive theory gives a reasonable prediction of the experiments by introducing a reduction factor. The discrepancy in linear growth rates between the experiment and the prediction is amplified as the quasi-single-mode interface deviates more severely from the single-mode one. In the weakly nonlinear stage, the nonlinear model valid for a single-mode interface with small amplitude loses efficacy, which indicates that the effects of high-order modes on amplitude growth must be considered. For the saw-tooth interface with small amplitude, the amplitudes of the first three harmonics are extracted from the experiment and compared with the previous theory. The comparison proves that each initial mode develops independently in the linear and weakly nonlinear stages. A nonlinear model proposed by Zhang & Guo (*J. Fluid Mech.*, vol. 786, 2016, pp. 47–61) is then modified by considering the effects of high-order modes. The modified model is proved to be valid in the weakly nonlinear stage even for the cases with high initial amplitude. More high-order modes are needed to match the experiment for the interfaces with a more severe deviation from the single-mode one.

Key words: shock waves

1. Introduction

Richtmyer–Meshkov (RM) instability occurs when an initially perturbed interface separating two different fluids is impulsively accelerated by a shock wave (Richtmyer 1960; Meshkov 1969). It has become increasingly significant in many applications such as inertial confinement fusion (Lindl *et al.* 2014) and astrophysical problems

† Email address for correspondence: sanjing@ustc.edu.cn

https://doi.org/10.1017/jfm.2019.416 Published online by Cambridge University Press

(Shimoda *et al.* 2015). To understand this instability, extensive studies on the interaction of a shock wave with a perturbed interface have been performed, and several comprehensive reviews have been presented (Brouillette 2002; Ranjan, Oakley & Bonazza 2011; Zhou 2017*a*,*b*; Zhai *et al.* 2018).

Previous work mainly focused on the evolution of a single-mode interface because it is the basis for constituting complex interfaces and can be easily treated theoretically. A multi-mode interface can be regarded as a combination of numerous modes with different amplitudes and, therefore, it is expected that studies of the single-mode interface can facilitate understanding of the multi-mode counterpart. Numerous models including linear and nonlinear ones have been proposed to predict the growth rate of a single-mode interface (Richtmyer 1960; Zhang & Sohn 1997; Vandenboomgaerde, Gauthier & Mügler 2002; Mariani *et al.* 2008; Velikovich, Herrmann & Abarzhi 2014). After the shock passes through the single-mode interface, high-order harmonics grow from zero gradually and then interact with each other in the nonlinear stage. To predict the evolution of each mode and construct a transition from a linear growth at early times to a nonlinear one at late times, Zhang & Sohn (1996) proposed a fourth-order nonlinear solution based on the perturbation expansion, and the model validity range was then extended by a Padé approximation (Zhang & Sohn 1997). Vandenboomgaerde *et al.* (2002) proposed a similar approach with accurate approximations by retaining only the terms with the highest power in time. For the multi-mode case, Mikaelian (2005) pointed out that superposing each mode growth independently in the linear phase is allowable if the amplitude of each mode satisfies the small-amplitude prerequisite. Niederhaus & Jacobs (2003) also proved that the linear stability theory can provide excellent agreement for the individual mode amplitudes of multi-mode initial perturbations until the interface becomes multi-valued. In the weakly nonlinear phase, provided mode coupling is absent, Vandenboomgaerde *et al.* (2002) proposed a nonlinear model to predict the amplitude evolution of each mode of a multi-mode interface. At the late nonlinear phase, the coupling and competition effects between modes become more important such that the flow develops into a disordered state and no theory is available in this highly nonlinear regime. However, direct validations of perturbation or potential theory for a simple multi-mode interface going from the linear to nonlinear regimes are scarce but very desirable.

Previous models were proposed mainly for the interface satisfying the small-perturbation hypothesis. As the ratio of initial amplitude to wavelength (a_{i0}/λ) increases, new flow features and growth law of the amplitude will occur. For the single-mode interface, experiments with high initial amplitude and high shock Mach number were conducted by Dimonte *et al.* (1996) and Aleshin *et al.* (1997). The amplitude growth rate was found to deviate from the prediction by the impulsive model, and this was ascribed to compressible effects. However, Rikanati *et al.* (2003) and Sadot *et al.* (2003) believed the effect of the high initial amplitude on the instability evolution was overlooked in the analysis above. Rikanati *et al.* (2003) proposed a reduction factor to modify the impulsive theory for initial sinusoidal and chevron shaped interfaces with high amplitude. The model matches experiments with low Mach numbers (Rikanati *et al.* 2003) and also high Mach numbers (Dimonte *et al.* 1996; Aleshin *et al.* 1997). As a result, Rikanati *et al.* (2003) and Sadot *et al.* (2003) concluded that the high-amplitude effect is the dominant reason for the deviation of the experimental growth rate from the impulsive theory, even at high Mach numbers. For the multi-mode interface, Bakhrakh *et al.* (1995) experimentally investigated the differences between conjugated circle arcs, ‘step-like’ and ‘saw-tooth’

https://doi.org/10.1017/jfm.2019.416 Published online by Cambridge University Press

interfaces. The authors found that the growth rate of amplitude strongly depends on the interface shape, but this dependence flattens as a_{i0}/λ increases. In addition, inclined and 'chevron' gas interfaces were also investigated (McFarland, Greenough & Ranjan 2013; McFarland *et al.* 2014; Luo *et al.* 2016; Mohaghar *et al.* 2017; Guo *et al.* 2018), and high-amplitude effects of the initial interface on the shocked flow were discussed. It was concluded that the secondary compressible effect on the evolution of an interface with high initial amplitude is significant.

In this work, we design and generate four quasi-single-mode interfaces (the fundamental mode is the most significant one among all modes of the interface), including a circular-arc, a trapezoid, a square-waveform and a saw-tooth interface, aiming to assess the deviation degree of single-mode models for predicting the quasi-single-mode interface growth. For each interface, two initial amplitudes, one satisfying the small-perturbation hypothesis and the other not, are considered. The effects of high-order modes on the amplitude growth in linear and weakly nonlinear phases are evaluated, and the high-amplitude effects on the flow are also highlighted.

2. Experimental method

As indicated in figure 1, five different kinds of interfaces, including a single-mode (SM), a circular-arc (CA), a trapezoid (TR), a square-waveform (SW) and a saw-tooth (ST) interface, are involved. For each case, the wavelength (λ) is 60 mm and two initial amplitudes, one satisfying the small-perturbation hypothesis and the other not, are considered, respectively. The Fourier expansions of the quasi-single-mode interfaces with small initial amplitude are presented as follows:

$$\left.\begin{aligned} y_{CA} &= a_{i0}[-1.042\cos(kx) + 0.051\cos(3kx) - 0.011\cos(5kx) + \cdots], \\ y_{TR} &= a_{i0}[-1.163\cos(kx) + 0.159\cos(3kx) + 0.034\cos(5kx) - \cdots], \\ y_{SW} &= a_{i0}[-1.273\cos(kx) + 0.424\cos(3kx) - 0.255\cos(5kx) + \cdots], \\ y_{ST} &= a_{i0}[-0.811\cos(kx) - 0.090\cos(3kx) - 0.032\cos(5kx) - \cdots], \end{aligned}\right\} \tag{2.1}$$

where y_{CA}, y_{TR}, y_{SW} and y_{ST} represent the Fourier expansions of the circular-arc, trapezoid, square-waveform and saw-tooth interfaces, respectively. The Fourier expansions of the quasi-single-mode interfaces with high initial amplitude are the same as those of interfaces with small initial amplitudes except the circular-arc one. In this work, the Fourier expansion of the circular-arc interface with high initial amplitude is $y_{CA} = a_{i0}[-1.134\cos(kx) + 0.188\cos(3kx) - 0.084\cos(5kx) + \cdots]$. One can observe that the fundamental mode for all the four quasi-single-mode interfaces is the most significant one among all the modes, which means the fundamental mode will dominate the interface evolution. For the square-waveform interface, although the third mode has an amplitude which is nearly 33 % of its fundamental mode, the amplitude ratio of the superposition of the fundamental mode with the third mode over the fundamental mode is 94 %. As a result, the fundamental mode still dominates. It can be found that some of the high-order modes in circular-arc, trapezoid and square-waveform interfaces are opposite to the fundamental mode in sign, and the deviation degree of these three interfaces from the single-mode one increases successively. For the saw-tooth interface, differently, the signs of the high-order modes are the same as the fundamental one.

To create the initial interface, taking the saw-tooth interface as an example as shown in figure 2(*a*), two transparent devices with a width of 140 mm are first manufactured using acrylic plates with a thickness of 3 mm. For the single-mode and circular-arc interfaces, the adjacent boundaries are carefully engraved to be of a

https://doi.org/10.1017/jfm.2019.416 Published online by Cambridge University Press

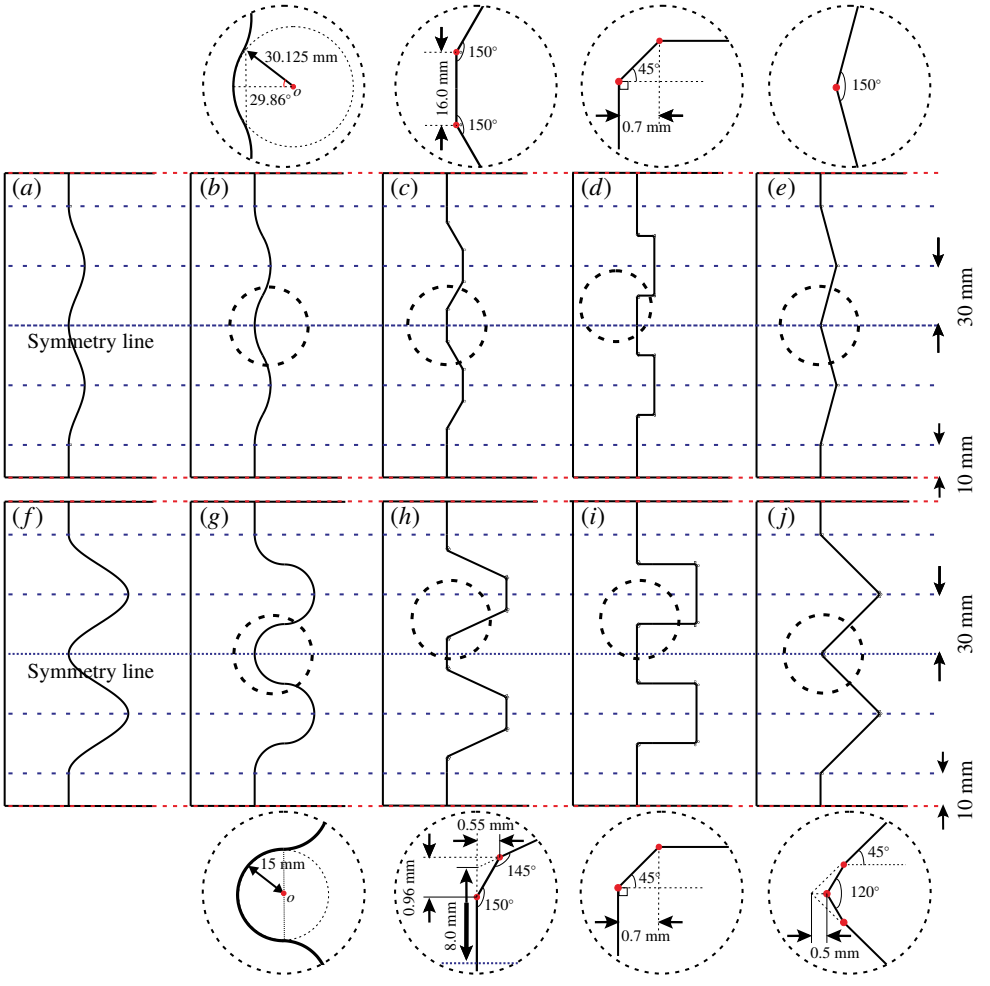


FIGURE 1. (Colour online) Schematics of initial interface configurations. The top and bottom rows correspond to the interfaces with small and high initial amplitudes, respectively. The interface shapes from the left to the right are single-mode, circular-arc, trapezoid, square-waveform and saw-tooth, respectively. Enlargement figures show the details of the interface. The dot represents a thin pin with a diameter of 0.148 mm to avoid the pressure singularity at the vertex. The incident shock moves from the left to the right.

single-mode or circular-arc shape with a depth of 0.2 mm. To restrict the soap film to the designed shape, two thin filaments with a thickness of 0.5 mm are normally attached to the inner surfaces of the upper and lower plates, respectively. Thus the filament protrusion is only 0.3 mm, having a negligible influence on the flow. The shape of the circular-arc interface is created by pieces of symmetrical arcs, and the curvature radius of each point on the interface is the same (30.125 mm and 15 mm for small and high initial amplitudes, respectively). For the other three interfaces, to avoid the pressure singularity caused by surface tension at the vertex (Wang, Si & Luo 2013), thin pins with a diameter of 0.148 mm are arranged at the vertex to restrict the soap films. For each vertex, the number of pins is dependent on the

https://doi.org/10.1017/jfm.2019.416 Published online by Cambridge University Press

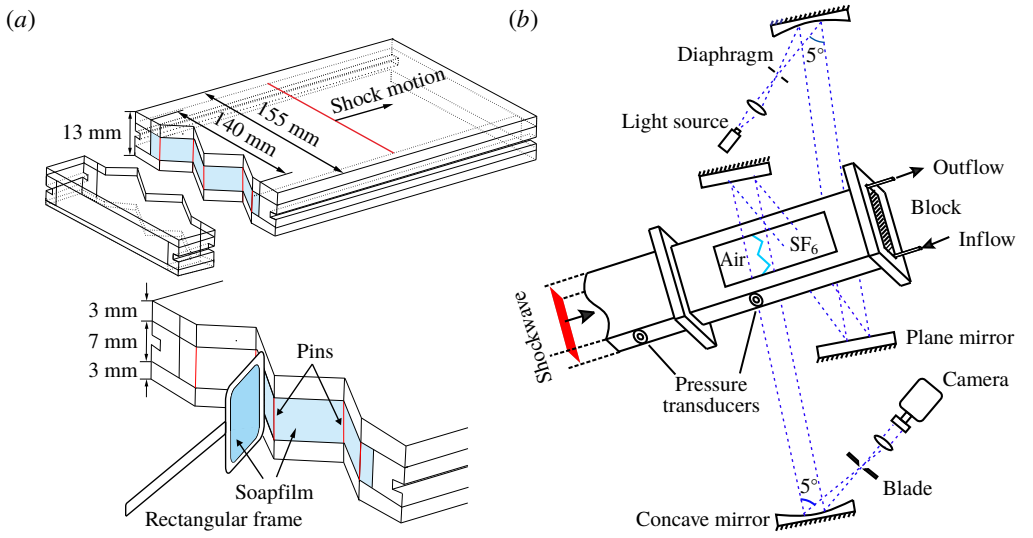


FIGURE 2. (Colour online) Schematics of the creation of a saw-tooth interface (*a*) and the schlieren photography adopted in the experiment (*b*).

vertex angle. For the saw-tooth and trapezoid interfaces with small initial amplitude, only one pin is used. For the trapezoid interface with high initial amplitude and the two square-waveform interfaces, two pins are used at each vertex. For the saw-tooth interface with high initial amplitude, three pins are used. The effects of pins at the vertex on the shock wave movement, interface morphology and the vorticity deposition have been investigated in previous work (Wang *et al.* 2013; Zhai *et al.* 2014) by experiments and numerical simulations. The results have proved that the pins have little influence on the interface morphology and vorticity deposition. Note that in previous work (Sadot *et al.* 1998; Jourdan & Houas 2005; Vandenboomgaerde *et al.* 2018) a wire mesh was generally used to hold an interface. The pins have similar drawbacks to the wire mesh. For example, the pins will enhance the mixing near the vertex, supporting a modest increase in amplitude growth rate (Prasad *et al.* 2000), and also will introduce short-wavelength perturbations to the initial interface (Vandenboomgaerde *et al.* 2018). However, compared with the wire mesh which will block the flow significantly, the pins have limited effects on the flow because they are only placed at each vertex. Although the pins may influence the high-order modes, they have negligible effect on the fundamental mode (Vandenboomgaerde *et al.* 2018). As a result, the effects of the pins in the present work are ignored since the fundamental mode is dominant.

Prior to the interface formation, the filaments or the edges of the acrylic plates are properly wetted by soap solutions (made of 78 % distilled water, 2 % sodium oleate and 20 % glycerine in mass). Then, a rectangular frame, the edges of which have been dipped into an appropriate amount of soap solutions, is pulled along the filaments or the edge of the acrylic plates. A soap film interface with the designed shape is then generated on the surface. Subsequently, the auxiliary framework is gently inserted until it is completely connected to the corresponding device. After that, the framework with soap film on its surface is slowly inserted into the test section. To form an air/SF_6 interface, air at the right-hand side of the interface must be replaced by SF_6 prior to the experiment. For this purpose, SF_6 is injected into the test section through an

https://doi.org/10.1017/jfm.2019.416 Published online by Cambridge University Press

'Inflow' hole, and air is gradually exhausted through an 'Outflow' hole, as shown in figure 2(*b*). A gas concentration detector is placed at the 'Outflow' hole to monitor the purity of SF_6 at the right-hand side of the interface. In the experiment, when the volume fraction of the oxygen measured by the detector is lower than 0.5 %, the gas inflation is stopped. Then the experiment is conducted as soon as possible to reduce the gas diffusion. In fact, during the gas inflation process, the gas exchange through the interface has already begun, and the gas inflation time influences the purity of gases. Moreover, after the gas inflation ends and before the experiments starts, the time interval also allows gas diffusion. These time intervals are difficult to keep exactly the same for different experimental runs. As a result, the gas components at both sides of the interface will vary a little from run to run, and the shock velocity will change when it enters the test section although the shock tube facility has a good repeatability. The gas components at both sides are determined by the shock velocities and one-dimensional (1-D) gas dynamics theory as given in table 1, in which $A = (\rho_2 - \rho_1)/(\rho_2 + \rho_1)$ is Atwood number with ρ_2 and ρ_1 being the densities of gases at the right- and left-hand sides of the interface, respectively. In our work, more than one successful experimental run was performed for each case. In table 1, the subscript s and h correspond to the interfaces with small and high initial amplitudes, respectively. The numbers 1 and 2 represent the typical experimental runs, respectively.

Experiments are conducted in the same shock tube as previous work (Liu *et al.* 2018). The cross-sectional area of the test section is 140 mm × 13 mm. As a result, the interface height is 7.0 mm because there is an acrylic plate with a thickness of 3 mm at each side in the test section. Note that the actual height of the single-mode and circular-arc interfaces is 6.4 mm because these two interfaces are restricted by the filaments with a 0.3 mm protrusion inside the flow field. The incident shock Mach number measured by piezoelectric transducers mounted in the driven section is 1.20 ± 0.03 from all the measurements, which indicates that the shock tube facility has a very good repeatability. Illuminated by a continuous light source (CEL-HXF300, maximum power output 249 W), the shocked flow is captured by high-speed schlieren photography as shown in figure 2(*b*). The frame rate of the camera (FASTCAM SA5, Photron Limited) is 50 000 f.p.s., and the exposure time is 0.37 μs. The spatial resolution of the schlieren image is 0.28 mm pixel^{-1}. The ambient pressure and temperature are 101.3 kPa and 293 K, respectively.

The three-dimensional (3-D) effect of a single-mode interface formed by the soap film technique has been discussed in our previous work (Luo, Wang & Si 2013). Because the gases on both sides of the interface are at ambient pressure, the soap film interface formed has a zero mean curvature and the geometry can be characterized as minimum surface (Isenberg 1992). In this work, for the two cases with small and high initial amplitudes, the wavelength λ is fixed at 60 mm, the amplitudes of the boundary slice are 4 and 15 mm, respectively. When the interface height is 20 mm, the amplitudes of the symmetry slices for the two cases are 2.48 and 8.42 mm, respectively. The amplitude ratios of the symmetry slice over the boundary slice are 62 % and 56 %, respectively, indicating a significant 3-D effect. When the interface height reduces to 7.0 mm, the amplitudes of the symmetry slices for the two cases are 3.75 and 14.00 mm, respectively. The amplitude ratios of the symmetry slice over the boundary slice are 93.75 % and 93.33 %, respectively. As a result, it is believed that the reduction of the interface height can reduce the 3-D effect, and the 3-D effect in this work is insignificant.

After the incident shock with Mach number of 1.2 impacts the interface, the flow behind the transmitted shock can be regarded as laminar and incompressible. As a

https://doi.org/10.1017/jfm.2019.416 Published online by Cambridge University Press

Case	a_{i0} (mm)	a_{i0}/λ	MF_1 (%)	MF_2 (%)	A	A^+	v_i (m s^{-1})	v_t (m s^{-1})	Δv (m s^{-1})
SM_s no. 1	4.0	0.067	71.5	94.4	0.54	0.57	355.1	189.9	70.5
SM_s no. 2	4.0	0.067	75.0	94.5	0.55	0.58	362.3	190.5	72.4
SM_h no. 1	15.0	0.250	94.7	95.0	0.60	0.63	408.1	195.8	73.0
SM_h no. 2	15.0	0.250	79.1	91.0	0.53	0.55	378.0	205.5	79.6
CA_s no. 1	4.0	0.067	91.1	90.1	0.55	0.57	396.2	207.2	75.7
CA_s no. 2	4.0	0.067	72.6	91.3	0.51	0.54	360.9	200.5	76.0
CA_h no. 1	15.0	0.250	68.0	95.2	0.53	0.56	355.0	192.0	73.4
CA_h no. 2	15.0	0.250	99.1	90.3	0.56	0.59	416.7	211.9	80.3
TR_s no. 1	4.0	0.067	87.9	94.5	0.58	0.61	385.7	190.5	69.2
TR_s no. 2	4.0	0.067	84.7	97.4	0.61	0.63	376.8	180.3	66.9
TR_h no. 1	15.0	0.250	87.6	92.7	0.56	0.59	388.5	198.0	72.2
TR_h no. 2	15.0	0.250	92.2	91.4	0.56	0.59	397.8	203.2	73.1
SW_s no. 1	4.3	0.072	84.0	94.0	0.57	0.60	380.3	193.0	71.7
SW_s no. 2	4.3	0.072	84.5	96.0	0.59	0.62	381.4	187.1	70.3
SW_h no. 1	15.0	0.250	91.1	94.6	0.59	0.62	393.2	191.7	69.7
SW_h no. 2	15.0	0.250	90.8	95.4	0.60	0.63	392.8	189.2	67.6
ST_s no. 1	4.0	0.067	84.0	96.8	0.60	0.62	376.8	182.7	67.6
ST_s no. 2	4.0	0.067	92.7	97.4	0.63	0.65	393.7	181.4	64.8
ST_h no. 1	14.5	0.242	93.0	93.2	0.58	0.61	397.2	196.4	70.5
ST_h no. 2	14.5	0.242	95.9	94.1	0.60	0.62	401.9	193.4	69.2

TABLE 1. Experimental initial parameters for all cases: a_{i0} is the initial amplitude of the interface; MF_1 (MF_2) is the mass fraction of air (SF_6) at the left (right) side of the interface; $A = (\rho_2 - \rho_1)/(\rho_2 + \rho_1)$ is pre-shock Atwood number with ρ_2 and ρ_1 being the densities of gases at the right and left sides of the interface, respectively; A^+ is post-shock Atwood number; v_i is the velocity of the incident shock; v_t is the velocity of the transmitted shock; Δv is the velocity of post-shock flow. The subscripts s and h correspond to the interfaces with small and high initial amplitudes, respectively. The numbers no. 1 and no. 2 represent the typical experimental runs, respectively.

result, the displacement thickness of the boundary layer (δ^*) can be approximately calculated by the following expression:

$$\delta^* = 1.72\sqrt{\frac{\mu x}{\rho \Delta v}}, \tag{2.2}$$

where x (= 100 mm measured from experiment) is the maximum distance that the interface moves when image recording ends. For simplification, the parameters of pure air as ambient gas and pure SF_6 as test gas at a temperature of 293 K are adopted for estimation. Thus, $\mu = 1.83 \times 10^{-5}$ Pa s ($= 1.60 \times 10^{-5}$ Pa s) is the viscosity coefficient of pure air (SF_6) and $\rho = 1.204$ kg m^{-3} ($= 6.143$ kg m^{-3}) is the density of pure air (SF_6); Δv ($\sim$70.0 m s^{-1}) is the post-shock flow velocity calculated from 1-D gas dynamics. According to (2.2), the displacement thickness of the boundary layer is calculated to be about 0.24 mm for ambient gas and 0.1 mm for test gas, which is much smaller than the inner height of the acrylic plates (7.0 mm). Therefore, the effect of the boundary layer on the interface evolution is negligible.

https://doi.org/10.1017/jfm.2019.416 Published online by Cambridge University Press

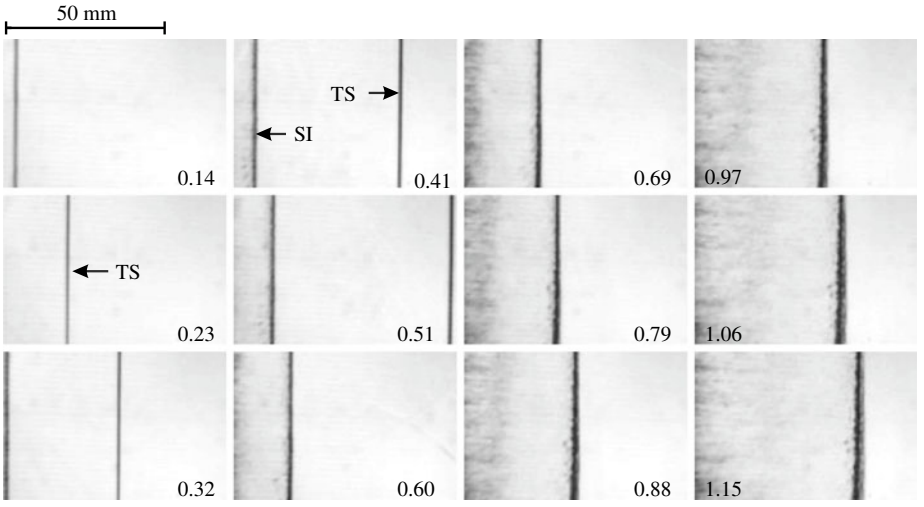


FIGURE 3. Schlieren pictures of a planar shock accelerating a planar air/SF_6 interface. TS, transmitted shock; SI, shocked interface. Incident shock with Mach number of 1.17 passes from left to right. The unit of the numbers is ms.

On the other hand, the motion and morphology of a planar interface after a planar shock impact can be used to evaluate the boundary layer effect. Figure 3 shows the typical evolution of a planar interface impacted by a planar shock performed in this shock tube. After shock impact, the transmitted shock TS and the shocked interface SI move uniformly. Table 2 shows the comparison of experimental results with their theoretical counterparts in the 1-D shock–interface interaction for four different runs. Both the velocities of the TS and the SI agree well between the experiments and the predictions, which means that the interface motion is not influenced significantly by the boundary layer effect, because the boundary layer will accelerate the interface motion (Morgan *et al.* 2012). Moreover, the growth of the planar interface thickness is mainly ascribed to the boundary layer effect (Brouillette & Sturevant 1993; Vetter & Sturtevant 1995). Therefore, the growth rate of the planar interface thickness can reflect the boundary layer effect. The larger the growth rate, the more significant the boundary layer effect (Brouillette & Sturevant 1993; Vetter & Sturtevant 1995). The growth rate of the planar interface thickness in case I^a in Vetter & Sturtevant (1995) was 0.94 m s^{-1}, and the authors concluded that the effects of shock-wave/boundary-layer interaction have been reduced significantly. In our shock tube, the initial conditions in Case 1 are similar to previous work, and the growth rate of the planar interface thickness is calculated as 0.84 m s^{-1}, which is even smaller than that in previous work. Therefore, it is believed that the boundary layer effect in this work is not significant.

3. Interfacial morphology and wave pattern

The experimental schlieren images for the five air/SF_6 interfaces with small and high initial amplitudes interacting with a planar shock are presented in figures 4 and 5, respectively. To improve the spatial and temporal resolutions, the images are presented with only one wavelength because the interface is periodic and one wavelength can represent the ensemble. For all cases, the moment when the shock

https://doi.org/10.1017/jfm.2019.416 Published online by Cambridge University Press

Case	*Ma*	v^t_{exp} (m s^{-1})	v^t_{the} (m s^{-1})	v^{si}_{exp} (m s^{-1})	v^{si}_{the} (m s^{-1})
1	1.17	171.4	170.5	61.5	59.9
2	1.21	175.0	176.5	71.8	72.0
3	1.21	175.3	176.5	71.5	72.0
4	1.21	173.6	176.5	71.9	72.0

TABLE 2. Comparison of experimental and theoretical parameters in the 1-D shock–interface interaction. *Ma*, incident shock Mach number, v^t_{exp} and v^t_{the} respectively represent the experimental and theoretical transmitted shock velocities, v^{si}_{exp} and v^{si}_{the} respectively represent the experimental and theoretical shocked interface velocities.

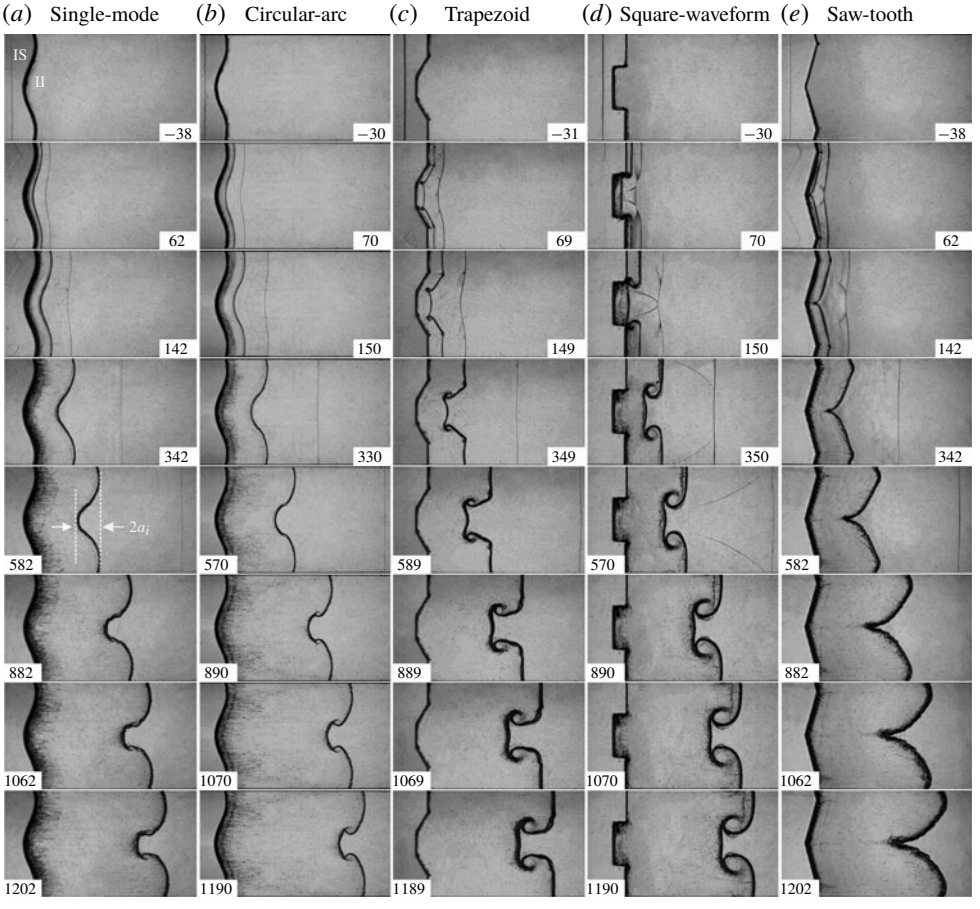


FIGURE 4. Schlieren pictures of interfaces with small initial amplitude accelerated by a planar shock wave: single-mode (*a*), circular-arc (*b*), trapezoid (*c*), square-waveform (*d*) and saw-tooth (*e*). Here, a_i, interface amplitude; IS, incident shock; II, initial interface. Numbers denote the time in μs.

contacts the interface centre is defined as the initial time ($t = 0$). From the interface morphologies, no obvious 3-D features are observed in the flow, which also indicates that 3-D effects can be ignored.

https://doi.org/10.1017/jfm.2019.416 Published online by Cambridge University Press

For the single-mode interface with small initial amplitude as shown in figure 4(*a*), the incident shock bifurcates into a downstream-moving transmitted shock and an upstream-moving reflected shock after it passes through the initial interface. The interface deforms gradually because of the pressure perturbations and the baroclinic vorticity induction. At the early stage, the spike (the heavier fluid penetrating into the lighter fluid) and the bubble (the lighter fluid penetrating into the heavier fluid) grow symmetrically (342 μs), indicating a linear growth of the amplitude. As the interface evolves, the high-order harmonics are generated and become significant, destroying the symmetry of the interface evolution (582 μs). Later, the spike starts to roll up and a pair of small vortices appears on its shoulder (1062 μs). Note that the interface morphology captured in the present study is more accurate than previous membrane results (Mariani *et al.* 2008). The spike head in this work is flat, which is consistent with the observation in membrane experiments (Mariani *et al.* 2008; Vandenboomgaerde *et al.* 2014), but is different from the previous membraneless experiments (Jones & Jacobs 1997; Collins & Jacobs 2002; Jacobs & Krivets 2005) in which the spike head is 'mushroom-like'. As Vandenboomgaerde *et al.* (2014) stated, the RM typical 'mushroom-like' structures on the interface are only made possible due to a diffusion layer at the initial interface. As illustrated in figure 4(*b*), both interface deformation and wave patterns in the circular-arc interface are similar to those in the single-mode case. Differently, the vortices are generated earlier in the circular-arc interface (∼570 μs) relative to the single-mode counterpart (∼882 μs) because the incident angle θ (the angle of the shock front with the interface) on the circular-arc interface surface (29.86°) is greater than that on the single-mode interface surface (22.73°), and the amplitude of vorticity deposited is proportional to $\sin\theta$. Also, the spike head in the circular-arc case is approximately 'mushroom-like' due to its larger initial interface curvature.

Figure 4(*c*) shows the evolution of the shocked trapezoid interface. Two pairs of Mach reflections occur on the transmitted shock, resulting in the formation of two Mach stems and four triple points (69 μs). The disturbed transmitted shock consists of two Mach stems and a flat part, and quickly recovers to a planar one (349 μs). The vortices are quickly produced from the vertex (69 μs), and are more obvious due to the larger incident angle (30°). A crater is observed on the spike head between a pair of vortices due to the velocity difference between the vortices and the flat part. The depth of the crater first increases (before 589 μs), and then reduces until it disappears. An opposite direction crater with a smaller curvature is observed on the bubble head (149–589 μs), and this crater also disappears gradually. Similarly to the trapezoid interface, Mach reflection occurs and a pair of Mach stems is formed (70 μs) in the square-waveform case as presented in figure 4(*d*). The bubble structure is quite flat relative to other interfaces. Because the incident angle is 90° for the square-waveform interface, the vortices produced the vertexes are more obvious.

The evolution of a shocked saw-tooth interface is shown in figure 4(*e*). Different from the work of Luo *et al.* (2016), the saw-tooth interface is periodic in this work, and the effect of flat parts on both sides of the perturbed interface on the evolution is eliminated (Luo *et al.* 2019). As the incident shock moves along two straight interfaces, Mach reflection occurs quickly on the transmitted shock, and the triple point and Mach stem are clearly observed at $t = 62$ μs. As the interface develops, the bubble becomes 'arc-like' while the spike becomes sharper (582–1202 μs). The vortices appear at very late time, which is partially ascribed to the very small incident angle (15°) in this case. Also, the pins used to form the vertex of the saw-tooth interface enhance the mixing near the spike head, covering the appearance of vortices (Prasad *et al.* 2000).

https://doi.org/10.1017/jfm.2019.416 Published online by Cambridge University Press

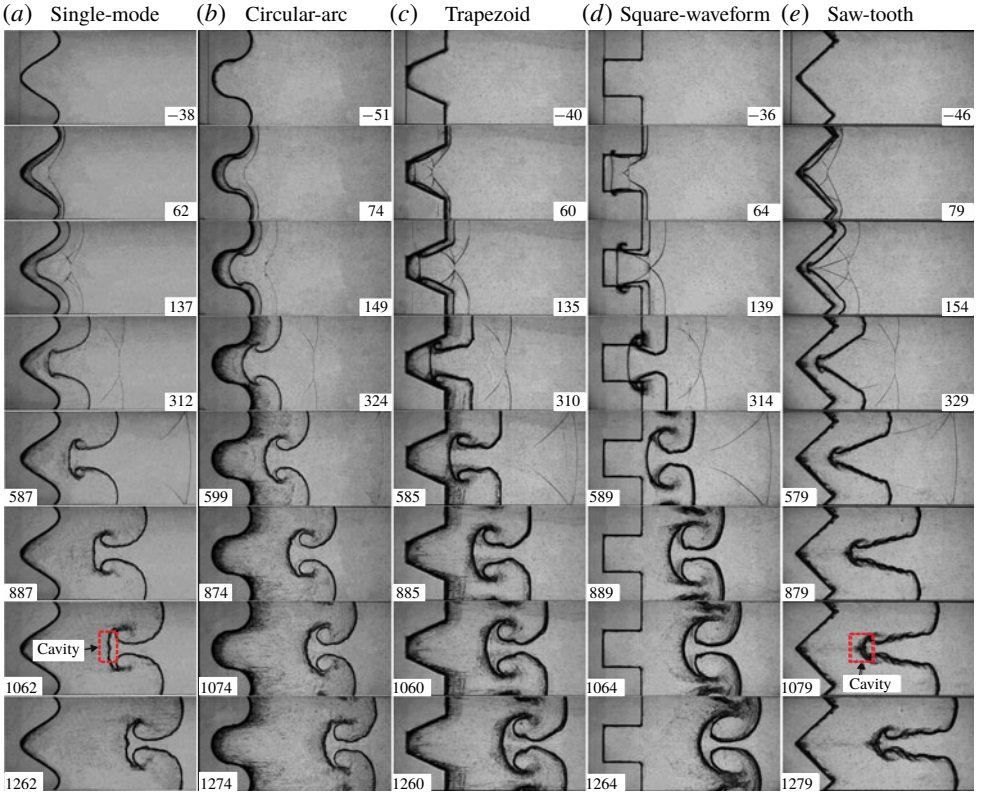


FIGURE 5. (Colour online) Schlieren pictures of interfaces with high initial amplitude accelerated by a planar shock wave: single-mode (*a*), circular-arc (*b*), trapezoid (*c*), square-waveform (*d*), and saw-tooth (*e*).

Figure 5 presents the evolutions of the five kinds of interfaces with high initial amplitude. For the single-mode case as presented in figure 5(*a*), after the incident shock collides with the perturbed interface, Mach stems and triple points are formed on the transmitted shock (62 μs). The wave patterns are more complicated compared with the case with small initial amplitude, and the secondary compressible effect becomes more significant for the high initial amplitude (McFarland *et al.* 2013). As the initial amplitude increases while the wavelength remains the same, the curvature radius of the spike head decreases. The shape of the spike head gradually converts from circular-arc to flat (587 μs) and a cavity even occurs at the spike centre (887 μs). The scale of the cavity increases as the interface evolves. In the previous membraneless experiments (Jones & Jacobs 1997; Collins & Jacobs 2002; Jacobs & Krivets 2005) and high-amplitude single-mode interface experiments with membranes (Bakhrakh *et al.* 1995; Jourdan & Houas 2005; Vandenboomgaerde *et al.* 2014), the cavity has never been observed. To the best of the authors' knowledge, this is the first time that the cavity has been observed in an experiment. Note that the cavity was observed in numerical simulations by Holmes *et al.* (1999), and they stated that the formation of the cavity is due to the vorticity on the slip lines connected to the spike centre, which causes the different flow velocities. That is to say, the cavity is closely related to the very strong Mach reflection. Therefore, the cavity is not observed on

https://doi.org/10.1017/jfm.2019.416 Published online by Cambridge University Press

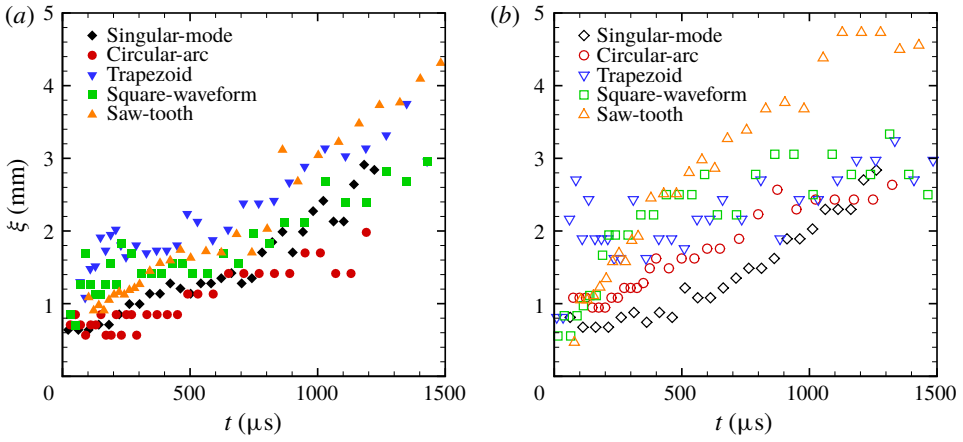


FIGURE 6. (Colour online) The thickness variation of the interface for small initial amplitude (*a*) and for high initial amplitude (*b*).

the circular-arc interface with high initial amplitude, as shown in figure 5(*b*), since the Mach reflection is weak in this case, and the little vorticity deposited on the slip lines does not obviously change the movement of the spike head. Relative to the single-mode case, the vortices in the circular-arc interface occur earlier and are more prominent.

The development of the trapezoid and square-waveform interfaces with high initial amplitude is given in figures 5(*c*) and 5(*d*). Compared with the cases with small initial amplitude, the wave patterns are more complicated and vortices are more prominent. A crater is also observed on the spike head for both cases. However, there is no obvious crater on the bubble head for the square-waveform interface. Both the spike and the bubble heads have a 'mushroom-like' shape, while they are quite flat for the cases with small amplitude. In the evolution of the saw-tooth interface, as shown in figure 5(*e*), except for the primary vortex pair at the spike head, many small vortices are also generated on both inclined boundaries which are ascribed to the RM and Kelvin–Helmholtz instabilities. A cavity is formed on the spike centre (1079 μs), and for the same reason as that in the single-mode case. Similarly, the cavity has been also observed in many numerical simulations (Hawley & Zabusky 1989; McFarland, Greenough & Ranjan 2011; Wang *et al.* 2012), but has never been found in previous experiments, probably due to the boundary layer effect on the initial interface (Wang *et al.* 2012; McFarland *et al.* 2014, 2015) or the wire mesh used to form the interface (Rikanati *et al.* 2003; Sadot *et al.* 2003). Our work provides the first experimental evidence for the existence of the cavity in the shocked saw-tooth interface.

From the schlieren pictures, one can observe that the interface has a thickness. After the shock impact, the soap films become atomized. Due to the lower energy deposited by the shock wave on the soap film droplets in this work, the atomization is less efficient. The mean radius of the droplets is about 59 μm with the shock Mach number of 1.2 according to the work of Ranjan *et al.* (2009). In addition, after the shock impact, the soap film is broken, and the gases at both sides diffuse quickly, forming an interface with a thickness. The interface thickness evolution is shown in figure 6 for each case. From the comparison, the interface appears significantly thicker in trapezoid, square-waveform and saw-tooth interface images. Several reasons may account for this change. Firstly, the thin pins used at each vertex to avoid

https://doi.org/10.1017/jfm.2019.416 Published online by Cambridge University Press

the pressure singularity in these three interfaces will enhance the mixing near the vertexes (Prasad *et al.* 2000), resulting in a thicker interface. Secondly, the thin pins will somewhat impede the interface movement and increase its thickness. Thirdly, for these three interfaces, the initial interface height is 7.0 mm. However, for the single-mode and circular-arc interfaces, the actual initial interface height is 6.4 mm, as described above. More soap film droplets may result in a thicker interface. As the interface develops, the initially invisible small perturbations on the interface will also develop. Although these small perturbations have limited effects on the interface morphology, their development will increase the interface thickness. As a result, the interface thickness grows gradually for all cases.

4. Amplitude growth in the linear stage

The experimental linear growth rates of different interfaces (v_{exp}) are obtained by linear fitting of the experimental data before the growth rate reduces. For single-mode interfaces, the previous work (Niederhaus & Jacobs 2003; Liu *et al.* 2018) indicated that the impulsive model (Richtmyer 1960) can provide an accurate prediction of amplitude growth rate of the interface when a_{i0}/λ is sufficiently small ($\leqslant 0.05$). However, when a_{i0}/λ is larger than 0.05, its prediction gradually deviates from the experiment as a_{i0}/λ increases (Rikanati *et al.* 2003; Dell *et al.* 2017). Therefore, in order to give an accurate prediction for the single-mode interface in this study, because the initial a_{i0}/λ is larger than 0.05, the impulsive model is modified by multiplying by a reduction factor R:

$$v_{the} = R\,k\Delta v A^{+} a_{i0}^{+}, \tag{4.1}$$

where v_{the} is the theoretical amplitude growth rate predicted by the modified impulsive model and $a_{i0}^{+} = a_{i0}(1 - \Delta v/v_s)$ is the post-shock amplitude. In this work, for the case with small initial amplitude, R is 0.9 which is approximately the theoretical value discussed by Buttler *et al.* (2012). However, for the case with high initial amplitude, R is 0.32 which is much smaller than the theoretical value (~ 0.7). The failure of the theory to predict the reduction factor for high initial amplitude is believed to be caused partially by ignorance of the secondary compressible effects. As a_{i0}/λ increases, secondary compressible effects (shocks reflected from the upper and lower initial interfaces as well as the walls) become stronger and more vorticity is deposited on the interface, resulting in the suppressed linear growth rate of the interface and the earlier appearance of nonlinear growth of the interface perturbation (McFarland *et al.* 2013). Based on the reduction factor R, both v_{exp} and v_{the} are listed in table 3 for all cases. Note that because the modified impulsive model can predict the single-mode interface evolution well, to highlight the deviation degree of the quasi-single-mode interface from the single-mode one, a_{i0} is still adopted in the theoretical prediction of the linear growth rate for all the quasi-single-mode interfaces. A ratio $\tilde{v}$, defined as $\tilde{v} = v_{exp}/v_{the}$, is also given in table 3 for each case. In fact, $\tilde{v}$ represents the deviation degree of the quasi-single-mode interface from the single-mode one. As the initial interface gradually deviates from the single-mode one, the discrepancy between the prediction and the experiment is amplified. Specifically, the model underestimates the growth rate of the saw-tooth interface, while overestimating the growth rate of the other three interfaces.

To illustrate the role of the fundamental mode in the linear stage, $1/c_1$, with c_1 being the coefficient of the fundamental mode in (2.1), is calculated and listed in table 3 for each case. The comparison of $1/c_1$ with $\tilde{v}$ indicates that although the

https://doi.org/10.1017/jfm.2019.416 Published online by Cambridge University Press

	Case	v_{exp} (m s^{-1})	v_{the} (m s^{-1})	$\tilde{v}$	$1/c_1$
For small amplitude	SM_s no. 1	12.05 ± 1.19	12.08	1.00 ± 0.10	1.00
	SM_s no. 2	12.63 ± 1.27	12.58	1.00 ± 0.10	1.00
	CA_s no. 1	12.03 ± 1.29	13.27	0.91 ± 0.10	0.96
	CA_s no. 2	11.32 ± 1.34	12.17	0.93 ± 0.10	0.96
	TR_s no. 1	11.80 ± 1.29	13.23	0.89 ± 0.10	0.86
	TR_s no. 2	12.02 ± 1.28	13.19	0.91 ± 0.10	0.86
	SW_s no. 1	10.88 ± 1.26	14.30	0.76 ± 0.09	0.79
	SW_s no. 2	11.41 ± 1.29	14.60	0.78 ± 0.09	0.79
	ST_s no. 1	15.40 ± 1.28	13.09	1.18 ± 0.10	1.23
	ST_s no. 2	16.03 ± 1.29	13.34	1.20 ± 0.10	1.23
	Case	v_{exp} (m s^{-1})	v_{the} (m s^{-1})	$\tilde{v}$	$1/c_1$
For high amplitude	SM_h no. 1	18.81 ± 1.31	19.12	0.98 ± 0.07	1.00
	SM_h no. 2	17.78 ± 1.27	17.50	1.02 ± 0.07	1.00
	CA_h no. 1	14.55 ± 1.17	16.47	0.88 ± 0.07	0.88
	CA_h no. 2	17.96 ± 1.39	19.36	0.93 ± 0.07	0.88
	TR_h no. 1	16.89 ± 1.21	17.45	0.97 ± 0.07	0.86
	TR_h no. 2	16.80 ± 1.21	17.63	0.95 ± 0.07	0.86
	SW_h no. 1	15.57 ± 1.25	17.81	0.87 ± 0.07	0.79
	SW_h no. 2	14.60 ± 1.20	17.63	0.83 ± 0.07	0.79
	ST_h no. 1	25.06 ± 1.26	17.13	1.46 ± 0.07	1.23
	ST_h no. 2	23.95 ± 1.26	17.36	1.38 ± 0.07	1.23

TABLE 3. Comparison of linear growth rate of different cases: v_{exp} is the experimental velocity obtained through linear fitting, v_{the} is the theoretical velocity calculated by the incompressible theory of Richtmyer (1960) and $\tilde{v} = v_{exp}/v_{the}$; c_1 is the coefficient of the fundamental mode in the Fourier expansion.

initial interface deviates from the single-mode one, the fundamental mode of the initial interface determines the linear growth rate in all cases because the fundamental mode is dominant, and the effects of high-order modes can be ignored in the linear stage.

5. Amplitude growth in the nonlinear stage

The amplitude growth as well as the evolutions of the spike and bubble are considered as shown in figures 7 and 8, respectively, for the small and high initial amplitude cases. The time is normalized by $kv_{exp}(t-t^*)$ with t^* being the characteristic time for the startup phase. According to Lombardini & Pullin (2009), t^* can be calculated by the following expression:

$$t^* = \frac{1}{2k}\left(\frac{1-A^+}{v_f+\Delta v}+\frac{1+A^+}{v_t-\Delta v}\right), \tag{5.1}$$

where v_f and v_t are the velocities of the reflected shock and transmitted shock, respectively. The amplitude is scaled as $k(a_i - a_i^*)$ where a_i^* is the corresponding experimental amplitude at t^*. For all cases, the values of t^* and a_i^* calculated from (5.1) are provided in table 4. In experiments, the centre of the material layer, defined as the average position of the two boundaries, is considered as the interface boundary, and the error bars result from the thickness of the material layer. The dimensionless

https://doi.org/10.1017/jfm.2019.416 Published online by Cambridge University Press

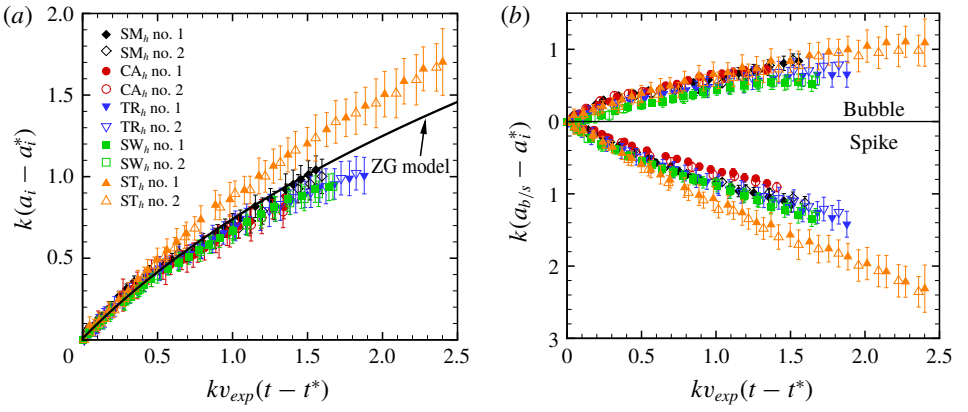


FIGURE 7. (Colour online) Comparisons of the dimensionless amplitude of the interface (*a*) and of the bubble and spike (*b*) for all interfaces with small initial amplitude.

Case	SM$_s$ no. 1	SM$_s$ no. 2	CA$_s$ no. 1	CA$_s$ no. 2	TR$_s$ no. 1	TR$_s$ no. 2	SW$_s$ no. 1	SW$_s$ no. 2	ST$_s$ no. 1	ST$_s$ no. 2
t^*	69.3	70.9	65.3	65.7	68.9	73.7	68.3	72.0	73.2	72.3
a_i^*	3.41	3.77	3.54	3.47	4.54	4.57	3.89	3.95	4.25	3.99
Case	SM$_h$ no. 1	SM$_h$ no. 2	CA$_h$ no. 1	CA$_h$ no. 2	TR$_h$ no. 1	TR$_h$ no. 2	SW$_h$ no. 1	SW$_h$ no. 2	ST$_h$ no. 1	ST$_h$ no. 2
t^*	68.0	66.8	69.4	61.4	68.1	62.1	70.6	66.5	71.5	67.2
a_i^*	12.4	12.3	12.7	12.5	13.4	13.4	12.9	12.8	13.5	13.4

TABLE 4. Values of t^* and a_i^* in all cases, and the units are μs and mm, respectively.

amplitude for different interfaces at the initial time is scaled at one point and the linear stage of perturbation growth is normalized. For the cases with small initial amplitude, as shown in figure 7(*a*), it can be found that the saw-tooth interface has the largest amplitude in the nonlinear stage (after dimensionless time about 0.5), while the other three quasi-single-mode interfaces have a smaller amplitude than the single-mode interface. This can be explained by their Fourier expansions. Compared with the single-mode interface, all the initial high-order modes in the saw-tooth interface have the same sign as the fundamental one and promote the perturbation growth, while the main high-order modes in the other three cases have an opposite sign to the fundamental one and inhibit the perturbation growth. However, for the cases with high initial amplitude, as shown in figure 8(*a*), the amplitude of the single-mode case seems relatively smaller than the quasi-single-mode interfaces. This amplitude reduction in the single-mode case is caused by the cavity formed at the spike head of the single-mode interface with high initial amplitude, as discussed before.

Comparisons of the dimensionless spike width (a_s) and the bubble width (a_b) are presented in figures 7(*b*) and 8(*b*). The dimensionless a_s of the saw-tooth interface is the largest among all cases because the curvature radius of the spike structure is infinitesimal. The dimensionless a_b for all cases are quite close to each other and increase gradually. For the trapezoid and square-waveform interfaces with small initial

https://doi.org/10.1017/jfm.2019.416 Published online by Cambridge University Press

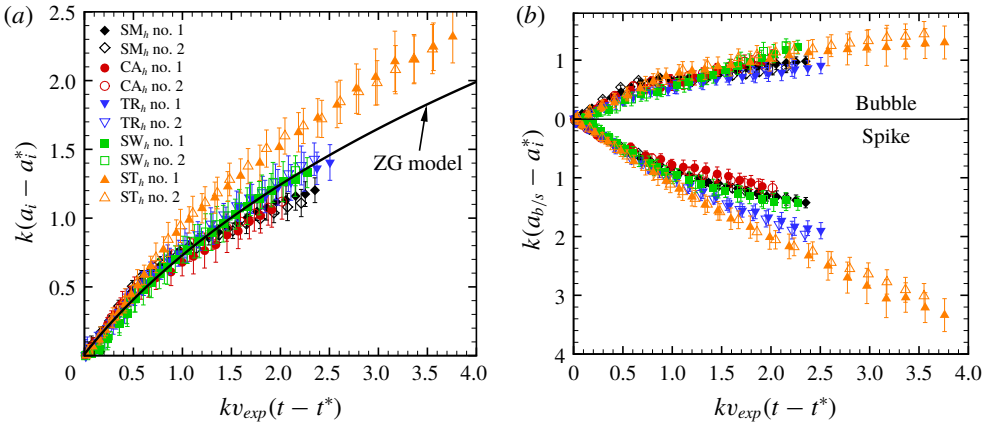


FIGURE 8. (Colour online) Comparisons of the dimensionless amplitude of the interface (*a*) and of the bubble and spike (*b*) for all interfaces with high initial amplitude.

amplitude, the dimensionless a_b is almost unvaried after the dimensionless time of 1.2. At the late time evolution, as shown in figures 4(*c*) and 4(*d*), the curvature radius of the bubble head is almost infinite. According to the relationship between the amplitude a_i and the curvature radius R_i of the interface, $1/(kR_i) = -\partial^2 a_i/\partial x^2$, the amplitude growth rate approaches zero when the the curvature radius is infinite.

The amplitude variations with time for the five cases are further compared with the prediction from the nonlinear model developed by Zhang & Guo (2016) (ZG model). For the single-mode interface evolution, the ZG model is expressed as

$$v(t) = \frac{v_{the}}{1 + \hat{a}kv_{the}t}, \tag{5.2}$$

where

$$\hat{a} = \frac{3}{4}\frac{(1+A^+)(3+A^+)}{[3+A^+ + \sqrt{2}(1+A^+)^{1/2}]}\frac{[4(3+A^+) + \sqrt{2}(9+A^+)(1+A^+)^{1/2}]}{[(3+A^+)^2 + 2\sqrt{2}(3-A^+)(1+A^+)^{1/2}]}, \tag{5.3}$$

with the positive Atwood number for bubbles and its negative counterpart for spikes with the same density ratio and $v(t)$ the growth rate at time t. As shown in figure 7(*a*) for the interfaces with small initial amplitude, the ZG model gives a good prediction for the evolution of the single-mode interface. However, the model slightly overestimates the growth of the circular-arc, trapezoid and square-waveform interfaces. A worse prediction of growth is observed for the saw-tooth interface because of the existence of a kink- singularity which will accelerate the spike growth. The failure of the model in predicting the behaviour of the quasi-single-mode interfaces indicates that it is necessary to evaluate the effect of initial high-order modes on the perturbation growth in the weakly nonlinear stage. For the interfaces with high initial amplitude, as shown in figure 8(*a*), the ZG model overestimates the growth of the single-mode interface in the nonlinear stage due to the formation of the cavity that reduces the amplitude. As a result, the failure of the model at late stages is caused partially by the secondary compressible effect. Occasionally, the ZG model works well for the trapezoid and square-waveform interfaces. One possible reason

https://doi.org/10.1017/jfm.2019.416 Published online by Cambridge University Press

is that the effects of initial high-order modes increase when the initial amplitude is large, and significantly change the growth rate.

For a single-mode interface, as the interface evolves, the fundamental mode will generate high harmonics. Zhang & Sohn (1997) proposed a model (ZS model) previously to predict the amplitudes of the first four harmonics. For a multi-mode interface, except for the fundamental mode, the high-order modes also exist on the initial interface. For an initially periodic interface, only odd-order modes exist on the initial interface. The even harmonics are generated as the interface develops from the initial odd-order modes and the coupling among them. Taking the first three harmonics in the present work for example, the fundamental and third modes exist on the initial interface. As the interface develops, the fundamental mode will generate the second and third harmonics. If mode coupling is considered, the coupling between the initial fundamental and third modes will also generate the second harmonic (Vandenboomgaerde *et al.* 2002; Di Stefano *et al.* 2015). To highlight the effects of high-order modes on amplitude growth, a Fourier analysis is performed here. Benefiting from the current method of interface formation, the high-quality schlieren pictures facilitate an accurate extraction of the interface contours with a simple image-processing program according to previous work (Liu *et al.* 2018). For the saw-tooth interface with small amplitude before the appearance of vortices, the amplitude growths of the first three harmonics are obtained from the experiment, as shown in figure 9. The amplitudes of the other higher harmonics from the experiment are neglected because they are quite small, and the errors are significant. For the first and second harmonics, the predictions from the ZS model are also given for comparison. The amplitude of the second harmonic in the experiment can be well predicted by the ZS model, which indicates that the second harmonic is generated only from the fundamental mode, and the coupling among initial fundamental and third modes is absent or weak enough that can be ignored during the time studied. For the third harmonic, except for the one initially existing on the interface, the one generated from the fundamental mode also contributes to the amplitude growth. For the amplitude of the third harmonic generated from the fundamental mode, the prediction from the ZS model shows that it maintains a very small value throughout the experiment duration, confirming the previous viewpoint (Liu *et al.* 2018) for the single-mode interface. The expression which was proposed to predict the amplitude of the first mode in the ZS model is also adopted to predict the amplitude of the initial third mode with the corresponding frequency, the initial amplitude $a_{i0}^{+}c_3$ and initial velocity $v_{exp}c_3$ with c_3 being the coefficient of the initial third mode in (2.1). Figure 9 shows that the prediction of the initial third mode from the ZS model coincides well with the experimental result. This fact also indicates that the initial odd-order modes develop independently, which agrees with the statement by Mikaelian (2005) that each mode will grow linearly and independently at early times before mode coupling becomes significant.

In figure 9, the global amplitude evolution from the experiment for the saw-tooth interface is also presented. Through comparison, one can find that the fundamental mode plays a dominant role in the amplitude growth. As the interface evolves, the discrepancy between the amplitude of the fundamental mode and the global amplitude is amplified, which means that the effects of the high-order modes on the amplitude growth must be considered. To predict the amplitude growth in the weakly nonlinear stage of the quasi-single-mode interface, the ZG model initially proposed for the single-mode interface is modified by considering the effects of high-order modes

https://doi.org/10.1017/jfm.2019.416 Published online by Cambridge University Press

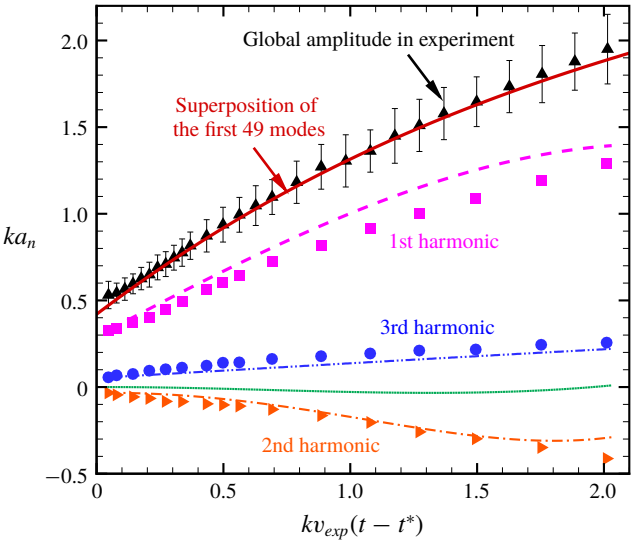


FIGURE 9. (Colour online) Perturbation amplitude variation of the first three harmonics for the saw-tooth interface with small initial amplitude. The symbols represent the experimental results. The dashed, dash-dot and dotted lines represent the predictions of the first, second and third harmonics from the ZS model, respectively. The dash-dot-dot line represents the prediction of the initial third mode from the ZS model.

according to the linear superposition principle proposed by Mikaelian (2005). The modified model (mZG model) can be expressed as

$$v = \sum_n \frac{c_{2n-1} v_{the}/c_1}{1 + (2n-1)\hat{a}kc_{2n-1} v_{the}/c_1 t}, \quad n = 1, 2, 3, \ldots. \tag{5.4}$$

Based on this model, the growth rate of each initial high-order mode can be obtained, and their linear superposition can result in the final growth rate of the quasi-single-mode interface. The predictions by the mZG model for the four quasi-single-mode interfaces with small and high initial amplitudes are presented in figure 10. In the present study, we choose to superimpose the smallest number modes to predict the experimental data until the prediction matches the experimental result (generally the difference between the prediction and the experiment is less than 3 %). For the cases with small initial amplitude, the superposition of the first three modes can give a reasonable prediction of the amplitude in experiment for the circular-arc interface, while a good prediction is only achieved for the saw-tooth interface after summing the first 49 modes. For the saw-tooth interface where only negative terms exist, adding more modes will not substantially alter the results after the prediction matches the experiment, i.e. the superposition over the modes converges asymptotically. For the interfaces where both positive and negative terms exist, after the prediction matches the experiment, adding more modes will alter the prediction, especially for the modes with relatively large coefficients. However, as the order of the mode increases, its coefficient becomes smaller and the effect on the prediction is gradually weakened. In other words, the superposition over the modes also converges but in an oscillatory way. For the cases with high initial amplitude,

https://doi.org/10.1017/jfm.2019.416 Published online by Cambridge University Press

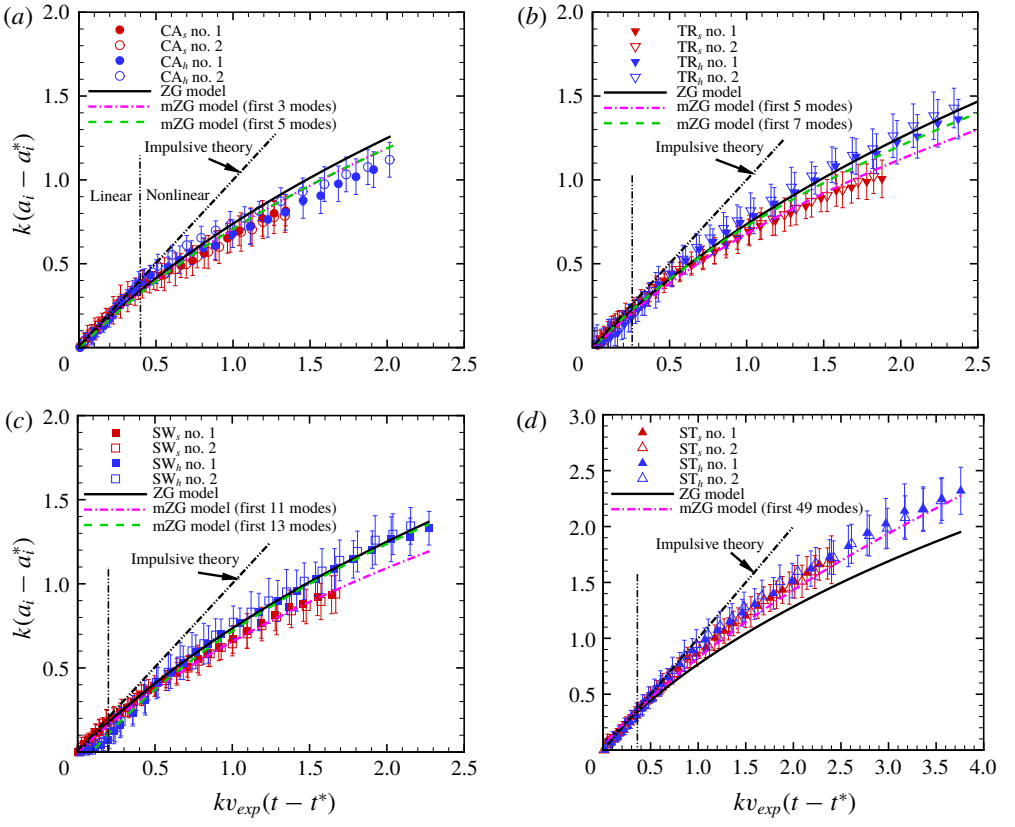


FIGURE 10. (Colour online) Comparison of the dimensionless amplitude in experiments with the prediction from the modified ZG model for the quasi-single-mode interfaces. Circular-arc (*a*), trapezoid (*b*), square-waveform (*c*) and saw-tooth (*d*).

generally, superimposing more modes is needed to match the experiment, because the effects of high-order modes are significant as a_{i0}/λ increases. More high-order modes needed in the model to match the experiment illustrates more severe deviation of the interface from the single-mode one. Although the ZG model fails to predict the amplitude of the single-mode interface with high initial amplitude at nonlinear stages, the superposition over the modes can still provide a satisfactory prediction of the experiment amplitude for the quasi-single-mode interfaces. For the square-waveform interface with high initial amplitude, note that the modelled growth rate does not start from the origin. The startup time in the experiment is so long ($\sim$200 μs) that equation (5.1) in invalid (the prediction is $\sim$70 μs), probably due to the complicated wave patterns in the square-waveform interface. As a result, the amplitude is predicted when the interface enters the linear phase in the experiment. The mZG model provides a satisfactory prediction of the experiments, which verifies that the coupling among different initial modes can be ignored when the fundamental mode is dominant as is the case in this work, especially for the small initial amplitude.

6. Conclusions

Shock-tube experiments on the Richtmyer–Meshkov instability of quasi-single-mode air/SF_6 interfaces are performed to evaluate the effects of high-order modes on the

https://doi.org/10.1017/jfm.2019.416 Published online by Cambridge University Press

amplitude growth in the linear and weakly nonlinear phases. A single-mode interface and four quasi-single-mode interfaces, including a circular-arc, a trapezoid, a square-waveform and a saw-tooth, are created by the soap film technique. For each case, two initial amplitudes, one satisfying the small-perturbation hypothesis and the other not, are also considered to highlight the effects of high amplitude.

For the single-mode interface with small initial amplitude, the present experiment provides clearer images than previous work. The spike head is flat, but not the 'mushroom-like' shape which is ascribed to the diffusion layer at the initial interface. For the trapezoid and square-waveform interfaces with small amplitude, vortices are quickly produced from the interface vertexes after the shock passage. Due to the velocity difference between the vortices and the post-shock flow, a crater is formed on the spike head as well as on the bubble head. The scale of the crater first increases and then reduces until it disappears. Finally, the heads of both the bubble and spike become quite flat. For the single-mode interface with high initial amplitude, a flat spike head is also observed and a cavity is even created. For the trapezoid and square-waveform interfaces with high amplitude, the crater is not obvious and the heads of both the bubble and spike are 'mushroom-like'. For the saw-tooth interface with high amplitude, a cavity is also observed at the spike head. We point out that the cavity observed in the single-mode and saw-tooth interfaces has been observed in previous numerical simulations, but has never previously been observed in experiments. This work provides the first experimental evidence of the cavity formation in the shocked interface.

The linear growth rates of the amplitude obtained from the experiments are compared with the predictions from the impulsive model with a reduction factor. As the interface shape gradually deviates from the single-mode one, the discrepancy between the experiment and the prediction is amplified. For the quasi-single-mode interfaces, the fundamental mode dominates the initial interface and, subsequently, determines the amplitude linear growth and high-order modes have negligible effect. In the nonlinear stages, for the interfaces with small amplitude, the nonlinear model which was proved to be applicable for single-mode interfaces loses efficacy for the quasi-single-mode interfaces, which indicates that the effects of high-order modes on the amplitude growth must be considered. Based on the accurate interface contour obtained, the amplitudes of the first three harmonics for the saw-tooth interface are extracted from the experiment and compared with the predictions from the ZS model (Zhang & Sohn 1997). The comparison proves that the coupling among different initial modes is so weak that it can be ignored. Therefore, each initial mode develops independently during the weakly nonlinear stage. As a result, the final growth rate of the quasi-single-mode interface can be obtained by linear superposition of the growth rate of each initial mode. Based on this principle, the nonlinear ZG model proposed by Zhang & Guo (2016) is modified by considering the effects of high-order modes to predict the growth rate of the quasi-single-mode interface. The modified nonlinear model is proved to be valid in the weakly nonlinear stages. For the single-mode interface with high amplitude, the ZG model fails at late stages due to the secondary compressible effects. Fortunately, the modified nonlinear model can also provide a satisfactory prediction of the amplitude of the quasi-single-mode interfaces with high initial amplitude. In the modified model, more high-order modes are needed to match the experiment as the deviation of the interface shape from the single-mode one is more pronounced.

https://doi.org/10.1017/jfm.2019.416 Published online by Cambridge University Press

Acknowledgements

This work was supported by the National Natural Science Foundation of China (nos. 11772329, 11625211 and 11621202), the Science Challenge Project (no. TZ2016001) and the Fundamental Research Funds for the Central Universities under grant no. WK2320000038.

REFERENCES

ALESHIN, A. N., LAZAREVA, E. V., CHEBOTAREVA, E. I., SERGEEV, S. V. & ZAYTSEV, S. G. 1997 Investigation of Richtmyer–Meshkov instability induced by the incident and reflected shock waves. In *Proceedings of the Sixth International Workshop on the Physics of Compressible Turbulent Mixing*, pp. 1–6. IUSTI, Universite de Provence.

BAKHRAKH, S., KLOPOV, B., MESHKOV, E., TOLSHMYAKOV, A. & YANILKIN, Y. 1995 Development of perturbations of a shock-accelerated interface between two gases. *J. Appl. Mech. Tech. Phys.* **36**, 341–346.

BROUILLETTE, M. 2002 The Richtmyer–Meshkov instability. *Annu. Rev. Fluid Mech.* **34**, 445–468.

BROUILLETTE, M. & STUREVANT, B. 1993 Experiments on the Richtmyer–Meshkov instability: small-scale perturbation on a plane interface. *Phys. Fluids* A **5**, 916–930.

BUTTLER, W. T., ORÓ, D. M., PRESTON, D. L., MIKAELIAN, K. O., CHERNE, F. J., HIXSON, R. S., MARIAM, F. G., MORRIS, C., STONE, J. B., TERRONES, G. *et al.* 2012 Unstable Richtmyer–Meshkov growth of solid and liquid metals in vacuum. *J. Fluid Mech.* **703**, 60–84.

COLLINS, B. D. & JACOBS, J. W. 2002 PLIF flow visualization and measurements of the Richtmyer–Meshkov instability of an air/SF_6 interface. *J. Fluid Mech.* **464**, 113–136.

DELL, Z. R., PANDIAN, A., BHOWMICK, A. K., SWISHER, N. C., STANIC, M., STELLINGWERF, R. F. & ABARZHI, S. I. 2017 Maximum initial growth-rate of strong-shock-driven Richtmyer–Meshkov instability. *Phys. Plasmas* **24** (9), 090702.

DI STEFANO, C. A., MALAMUD, G., KURANZ, C. C., KLEIN, S. R. & DRAKE, R. P. 2015 Measurement of Richtmyer–Meshkov mode coupling under steady shock conditions and at high energy density. *High Energy Dens. Phys.* **17**, 263–269.

DIMONTE, G., FRERKING, C. E., SCHNEIDER, M. & REMINGTON, B. 1996 Richtmyer–Meshkov instability with strong rdiatively driven shocks. *Phys. Plasmas* **3**, 614–630.

GUO, X., DING, J., LUO, X. & ZHAI, Z. 2018 Evolution of shocked multimode interface with sharp corners. *Phys. Rev. Fluids* **3**, 114004.

HAWLEY, J. F. & ZABUSKY, N. J. 1989 Vortex paradigm for shock-accelerated density-stratified interfaces. *Phys. Rev. Lett.* **63** (12), 1241–1244.

HOLMES, R. L., DIMONTE, G., FRYXELL, B., GITTINGS, M. L., GROVE, J. W., SCHNEIDER, M., SHARP, D. H., VELIKOVICH, A. L., WEAVER, R. P. & ZHANG, Q. 1999 Richtmyer–Meshkov instability growth: experiment, simulation and theory. *J. Fluid Mech.* **389**, 55–79.

ISENBERG, C. 1992 *The Science of Soap Films and Soap Bubbles*. Dover publications.

JACOBS, J. W. & KRIVETS, V. V. 2005 Experiments on the late-time development of single-mode Richtmyer–Meshkov instability. *Phys. Fluids* **17**, 034105.

JONES, M. A. & JACOBS, J. W. 1997 A membraneless experiment for the study of Richtmyer–Meshkov instability of a shock-accelerated gas interface. *Phys. Fluids* **9**, 3078–3085.

JOURDAN, G. & HOUAS, L. 2005 High-amplitude single-mode perturbation evolution at the Richtmyer–Meshkov instability. *Phys. Rev. Lett.* **95**, 204502.

LINDL, J., LANDEN, O., EDWARDS, J., MOSES, E. & TEAM, N. 2014 Review of the national ignition campaign 2009–2012. *Phys. Plasmas* **21**, 020501.

LIU, L., LIANG, Y., DING, J., LIU, N. & LUO, X. 2018 An elaborate experiment on the single-mode Richtmyer–Meshkov instability. *J. Fluid Mech.* **853**, R2.

LOMBARDINI, M. & PULLIN, D. I. 2009 Startup process in the Richtmyer–Meshkov instability. *Phys. Fluids* **21** (4), 044104.

LUO, X., DONG, P., SI, T. & ZHAI, Z. 2016 The Richtmyer–Meshkov instability of a 'V' shaped air/SF_6 interface. *J. Fluid Mech.* **802**, 186–202.

https://doi.org/10.1017/jfm.2019.416 Published online by Cambridge University Press

LUO, X., LIANG, Y., SI, T. & ZHAI, Z. 2019 Effects of non-periodic portions of interface on Richtmyer–Meshkov instability. *J. Fluid Mech.* **861**, 309–327.

LUO, X., WANG, X. & SI, T. 2013 The Richtmyer–Meshkov instability of a three-dimensional air/SF_6 interface with a minimum-surface feature. *J. Fluid Mech.* **722**, R2.

MARIANI, C., VANDENBOOMGAERDE, M., JOURDAN, G., SOUFFLAND, D. & HOUAS, L. 2008 Investigation of the Richtmyer–Meshkov instability with stereolithographed interfaces. *Phys. Rev. Lett.* **100**, 254503.

MCFARLAND, J. A., GREENOUGH, J. A. & RANJAN, D. 2011 Computational parametric study of a Richtmyer–Meshkov instability for an inclined interface. *Phys. Rev.* E **84** (2), 026303.

MCFARLAND, J. A., GREENOUGH, J. A. & RANJAN, D. 2013 Investigation of the initial perturbation amplitude for the inclined interface Richtmyer–Meshkov instability. *Phys. Scr.* **2013** (T155), 014014.

MCFARLAND, J. A., REILLY, D., BLACK, W., GREENOUGH, J. A. & RANJAN, D. 2015 Modal interactions between a large-wavelength inclined interface and small-wavelength multimode perturbations in a Richtmyer–Meshkov instability. *Phys. Rev.* E **92** (1), 013023.

MCFARLAND, J., REILLY, D., CREEL, S., MCDONALD, C., FINN, T. & RANJAN, D. 2014 Experimental investigation of the inclined interface Richtmyer–Meshkov instability before and after reshock. *Exp. Fluids* **55** (1), 1640–1653.

MESHKOV, E. E. 1969 Instability of the interface of two gases accelerated by a shock wave. *Fluid Dyn.* **4**, 101–104.

MIKAELIAN, K. O. 2005 Richtmyer–Meshkov instability of arbitrary shapes. *Phys. Fluids* **17**, 034101.

MOHAGHAR, M., CARTER, J., MUSCI, B., REILLY, D., MCFARLAND, J. & RANJAN, D. 2017 Evaluation of turbulent mixing transition in a shock-driven variable-density flow. *J. Fluid Mech.* **831**, 779–825.

MORGAN, R. V., AURE, R., STOCKERO, J. D., GREENOUGH, J. A., CABOT, W., LIKHACHEV, O. A. & JACOBS, J. W. 2012 On the late-time growth of the two-dimensional Richtmyer–Meshkov instabilities in shock tube experiments. *J. Fluid Mech.* **712**, 354–383.

NIEDERHAUS, C. E. & JACOBS, J. W. 2003 Experimental study of the Richtmyer–Meshkov instability of incompressible fluids. *J. Fluid Mech.* **485**, 243–277.

PRASAD, J. K., RASHEED, A., KUMAR, S. & STURTEVANT, B. 2000 The late-time development of the Richtmyer–Meshkov instability. *Phys. Fluids* **12**, 2108–2115.

RANJAN, D., NIEDERHAUS, J., OAKLEY, J., ANDERSON, M. & BONAZZA, R. 2009 Experimental investigation of shock-induced distortion of a light spherical gas inhomogeneity. In *Shock Waves*, pp. 1175–1180. Springer.

RANJAN, D., OAKLEY, J. & BONAZZA, R. 2011 Shock-bubble interactions. *Annu. Rev. Fluid Mech.* **43**, 117–140.

RICHTMYER, R. D. 1960 Taylor instability in shock acceleration of compressible fluids. *Commun. Pure Appl. Maths* **13**, 297–319.

RIKANATI, A., ORON, D., SADOT, O. & SHVARTS, D. 2003 High initial amplitude and high Mach number effects on the evolution of the single-mode Richtmyer–Meshkov instability. *Phys. Rev.* E **67**, 026307.

SADOT, O., EREZ, L., ALON, U., ORON, D., LEVIN, L. A., EREZ, G., BEN-DOR, G. & SHVARTS, D. 1998 Study of nonlinear evolution of single-mode and two-bubble interaction under Richtmyer–Meshkov instability. *Phys. Rev. Lett.* **80**, 1654–1657.

SADOT, O., RIKANATI, A., ORON, D., BEN-DOR, G. & SHVARTS, D. 2003 An experimental study of the high Mach number and high initial-amplitude effects on the evoltion of the single-mode Richtmyer–Meshkov instability. *Laser Part. Beams* **21**, 341–346.

SHIMODA, J., INOUE, T., OHIRA, Y., YAMAZAKI, R., BAMBA, A. & VINK, J. 2015 On cosmic-ray production efficiency at Supernova remnant shocks propagating into realistic diffuse interstellar medium. *Astrophys. J.* **803**, 98–103.

VANDENBOOMGAERDE, M., GAUTHIER, S. & MÜGLER, C. 2002 Nonlinear regime of a multimode Richtmyer–Meshkov instability: a simplified perturbation theory. *Phys. Fluids* **14** (3), 1111–1122.

https://doi.org/10.1017/jfm.2019.416 Published online by Cambridge University Press

VANDENBOOMGAERDE, M., ROUZIER, P., SOUFFLAND, D., BIAMINO, L., JOURDAN, G., HOUAS, L. & MARIANI, C. 2018 Nonlinear growth of the converging Richtmyer–Meshkov instability in a conventional shock tube. *Phys. Rev. Fluids* **3**, 014001.

VANDENBOOMGAERDE, M., SOUFFLAND, D., MARIANI, C., BIAMINO, L., JOURDAN, G. & HOUAS, L. 2014 An experimental and numerical investigation of the dependency on the initial conditions of the Richtmyer–Meshkov instability. *Phys. Fluids* **26**, 024109.

VELIKOVICH, A., HERRMANN, M. & ABARZHI, S. 2014 Perturbation theory and numerical modelling of weakly and moderately nonlinear dynamics of the incompressible Richtmyer–Meshkov instability. *J. Fluid Mech.* **751**, 432–479.

VETTER, M. & STURTEVANT, B. 1995 Experiments on the Richtmyer–Meshkov instability of an air/SF_6 interface. *Shock Waves* **4**, 247–252.

WANG, M., SI, T. & LUO, X. 2013 Generation of polygonal gas interfaces by soap film for Richtmyer–Meshkov instability study. *Exp. Fluids* **54**, 1427–1435.

WANG, T., LIU, J. H., BAI, J. S., JIANG, Y., LI, P. & LIU, K. 2012 Experimental and numerical investigation of inclined air/SF_6 interface instability under shock wave. *Z. Angew. Math. Mech.* **33** (1), 37–50.

ZHAI, Z., WANG, M., SI, T. & LUO, X. 2014 On the interaction of a planar shock with a light SF_6 polygonal interface. *J. Fluid Mech.* **757**, 800–816.

ZHAI, Z., ZOU, L., WU, Q. & LUO, X. 2018 Review of experimental Richtmyer–Meshkov instability in shock tube: from simple to complex. *Proc. Inst. Mech. Engrs* **232**, 2830–2849.

ZHANG, Q. & GUO, W. 2016 Universality of finger growth in two-dimensional Rayleigh–Taylor and Richtmyer–Meshkov instabilities with all density ratios. *J. Fluid Mech.* **786**, 47–61.

ZHANG, Q. & SOHN, S. I. 1996 An analytical nonlinear theory of Richtmyer–Meshkov instability. *Phys. Lett.* A **212**, 149–155.

ZHANG, Q. & SOHN, S. I. 1997 Nonlinear theory of unstable fluid mixing driven by shock wave. *Phys. Fluids* **9**, 1106–1124.

ZHOU, Y. 2017*a* Rayleigh–Taylor and Richtmyer–Meshkov instability induced flow, turbulence, and mixing. I. *Phys. Rep.* **720–722**, 1–136.

ZHOU, Y. 2017*b* Rayleigh–Taylor and Richtmyer–Meshkov instability induced flow, turbulence, and mixing. II. *Phys. Rep.* **723–725**, 1–160.

https://doi.org/10.1017/jfm.2019.416 Published online by Cambridge University Press